J. Fluid Mech. (1998), *vol.* 368, *pp.* 127–153. Printed in the United Kingdom

Unsteady convective exchange flows in cavities

By J. J. STURMAN AND G. N. IVEY

Centre for Water Research and Department of Environmental Engineering, University of Western Australia, Nedlands, Western Australia, 6907, Australia

(Received 7 January 1997 and in revised form 18 March 1998)

Horizontal exchange flows driven by spatial variation of buoyancy fluxes through the water surface are found in a variety of geophysical situations. In all examples of such flows the timescale characterizing the variability of the buoyancy fluxes is important and it can vary greatly in magnitude. In this laboratory study we focus on the effects of this unsteadiness of the buoyancy forcing and its influence on the resulting flushing and circulation processes in a cavity. The experiments described all start with destabilizing forcing of the flows, but the buoyancy fluxes are switched to stabilizing forcing at three different times spanning the major timescales characterizing the resulting cavity-scale flows. For destabilizing forcing, these timescales are the flushing time of the region of forcing, and the filling-box timescale, the time for the cavity-scale flow to reach steady state. When the forcing is stabilizing, the major timescale is the time for the fluid in the exchange flow to pass once through the forcing boundary layer. This too is a measure of the time to reach steady state, but it is generally distinct from the filling-box time. When a switch is made from destabilizing to stabilizing buoyancy flux, inertia is important and affects the approach to steady state of the subsequent flow. Velocities of the discharges from the end regions, whether forced in destabilizing or stabilizing ways, scaled as $u \sim (Bl)^{1/3}$ (where B is the forcing buoyancy flux and l is the length of the forcing region) in accordance with Phillips' (1966) results. Discharges with destabilizing and stabilizing forcing were, respectively, $Q_- \sim (Bl)^{1/3}H$ and $Q_+ \sim (Bl)^{1/3}\delta$ (where H is the depth below or above the forcing plate and δ is the boundary layer thickness). Thus $Q_-/Q_+ > O(1)$ provided $H > O(\delta)$, as was certainly the case in the experiments reported, demonstrating the overall importance of the flushing processes occurring during periods of cooling or destabilizing forcing.

1. Introduction

Horizontal exchange flows driven by spatial and temporal variation of buoyancy fluxes through the water surface are found in a variety of geophysical situations. Such exchange flows are found in oceans and lakes (e.g. Sturman, Ivey & Taylor 1996) and also in the atmosphere where sea-breezes are a common example (e.g. Reible, Simpson & Linden 1993). Our work is motivated by an interest in exchange flows in the sidearms of lakes, semi-enclosed seas and coastal ocean environments and, while we will focus on modelling these flows, there are broader applications arising from our work.

Similarity solutions for the steady circulation in semi-enclosed seas such as the Red Sea driven by uniform buoyancy flux across the surface were first proposed by Phillips (1966). He considered the case of uniform buoyancy flux B across the surface of a long, shallow box, with either positive or negative B, with a sill at the 'open' end of the box, so modelling the Straits of Bab-el-Mandeb at the southern end of the Red Sea. With either positive or negative B, the surface velocity of the water is proportional to $(Bx)^{1/3}$, where x is the distance from the virtual origin of the forcing zone. This widely cited

paper has spawned further work on the essential problem. Brocard & Harleman (1980) postulated a two-layer model of the recirculating flow, with the upper turbulent layer flow not exchanging mass or buoyancy across the interface between it and the lower laminar layer return flow, but with a mean flow turning at the closed end. Analytical solutions were derived by integrating the conservation equations vertically over each layer. One simple outcome of the model is that the surface velocity is independent of the length of the layer, contrary to the suggestion of Phillips (1966). Maxworthy (1997) affirmed that there was little or no mixing across the horizontal boundary between adjacent layers in a model for water bodies like the Red Sea, so adopting the basic postulate of Brocard & Harleman (1980).

Phillips (1966) also presented vertical buoyancy profiles from the Red Sea which showed no sharp gradients, implying the existence of a continuous downflow into the lower return flow. Assuming the buoyancy flux was proportional to water surface temperature, Jain (1982) formulated and solved similarity forms of the conservation equations which predicted the surface velocity to be directly proportional to the distance from the end. Both Brocard & Harleman (1980) and Jain (1982) concluded that their analytical results compared satisfactorily with Brocard & Harleman's (1980) experimental results. Møller (1984) compared field measurements in a fiord with his own laboratory experimental data and found discharges and therefore velocities consistent with Phillips' (1966) scaling. Phillips' (1966) model was revisited by Tragou & Garrett (1997), who proposed similarity forms of the turbulent eddy viscosity profiles. A consequence of matching the solutions to the field data was that the turbulent viscosity in the lower portion of the Red Sea took on very large values. When account was taken of bottom and sidewall friction (not in the model itself) the required high viscosities in the lower layer could not be fully accounted for and further work is required to resolve the issue of exchange flows of the Red Sea type.

A previous laboratory experimental study by Sturman *et al*. (1996) was conducted in a smaller facility at much lower Rayleigh number than for the present study. It was limited to an aspect ratio (channel height above the forcing region to length of forcing region) of one and focused on steady-state flows with destabilizing forcing. Work on convective flows induced by stabilizing forcing is exemplified by the laboratory experiments and numerical results of Coates & Patterson (1993), where the forcing flux was provided by penetrative radiation. The issue of time dependency in these exchange flows is important and clearly recognized, as for example in Tragou & Garrett (1997) where seasonal time dependency was discussed. On smaller timescales, diurnal changes in sign of the buoyancy flux across the air–water interface are important in lakes where exchange flows can be set up on diurnal timescales (Sturman *et al*. 1996). When we turn from lakes to larger scale bodies of water, time dependence on a seasonal or annual timescale is pertinent; this is the case for the Red Sea and similar large bodies of water (Phillips 1966; Tragou & Garrett 1996).

Typical magnitudes of sensible and latent surface heat fluxes in lakes are about 800 W m^{-2} (Monismith, Imberger & Morison 1990) and for mid-latitudes maximum daytime radiation fluxes into the water can be approximately 1000 W m^{-2}. Thus latent, sensible and radiant fluxes are of approximately the same magnitude. How they combine to produce a net positive or negative buoyancy flux is no simple matter, apart from the added complexities of wind stress and inflows and outflows (see Imberger 1994 for a discussion of the surface layer and associated energy fluxes). Furthermore, in locations such as the Red Sea and Shark Bay, Western Australia (e.g. Burling, Ivey & Pattiarachi 1996) for example, buoyancy fluxes can derive from increased salinity due to evaporation as well as from heat. In a lake, typically during the course of any

one day the buoyancy flux can have both positive and negative signs. In temperate latitudes during summer, the net heat flux is positive and the lake becomes stably stratified while during winter, the reverse is true and the lake tends to destratify.

In all examples the timescale of the variation of the forcing buoyancy fluxes is important and it can vary greatly from diurnal to annual. Our purpose in the present laboratory study is to provide insight into these varied convectively driven flows in the more complex field situations and, in particular, to focus on the affects of the unsteadiness of the buoyancy forcing and its influence on the resulting circulation and flushing processes.

2. Experimental apparatus and methods

The rectangular tank in which the experiments were conducted was thus designed to model horizontal exchange flows in which there was both a change in the sign of the forcing buoyancy fluxes with time and variations of the geometry of the forced regions. This change of sign of the buoyancy flux was addressed in the present laboratory experiments for the first time.

The tank was constructed of 19 mm Perspex sheet and insulated with 50 mm of polystyrene foam. The aspect ratio of tank height to tank length was $H/L = 0.05$ and the ratio of tank height to heated or cooled plate length (in the x-direction) was $H/l = 0.4$; see figure 1 for a schematic diagram. In addition to this basic configuration, Perspex inserts enabled contouring of the wall of the tank vertically opposite to the plates. This enables the effect of varying the aspect ratio H/l to be examined. The two-sided configuration of the tank was adopted in order to maintain control of the mean tank temperature and hence heat losses, although generally the geophysical flows being modelled were single sided.

Heat fluxes were applied by circulating water through jackets behind the horizontal copper plates located at the ends of the tank. We desired the copper plates to respond quickly to the temperature of the water in the jacket behind them. The thickness of the copper plates required to ensure structural integrity (3 mm) gave rise to a plate e-folding temperature response time of the order of 10 s after either startup or a switch in the sign of the buoyancy flux. The measured buoyancy flux attained 66 % of its final value after 23 s. The major timescales (except the formation time of the thermals, see equation (11) and associated discussion) are given by equations (12), (18), and (19) and (13) together. In each case the timescale is proportional to (or inversely proportional to) $B^{1/3}$. A variation of B by a factor of $2/3$ results in a variation of the timescales by a factor of 0.9. Given that we are interpreting our experimental results solely by scaling arguments, the variation of B seems unimportant. Notice too that the same is true for the destabilizing discharge (equation (13)) and for results for the stabilizing case. In all cases the starting conditions of our experiments were carefully measured. Note that our specified and controlled boundary conditions are constant temperature, but we measure the mean buoyancy flux, as this is more readily available to and of interest to researchers in the field.

Switching the sign of the buoyancy flux at the plates was made possible by using two mechanically connected four-way valves, which enabled heated and chilled water to be interchanged from one heat exchanger to the other. A typical plot of forcing buoyancy flux as a function of time is shown in figure 2, where the flux was calculated from the flow rate and temperature change of the water flowing through the heat exchangers behind the plates. These temperatures were measured by thermistors with a response time of about 1 s, calibrated to better than 0.01 °C against a platinum resistance

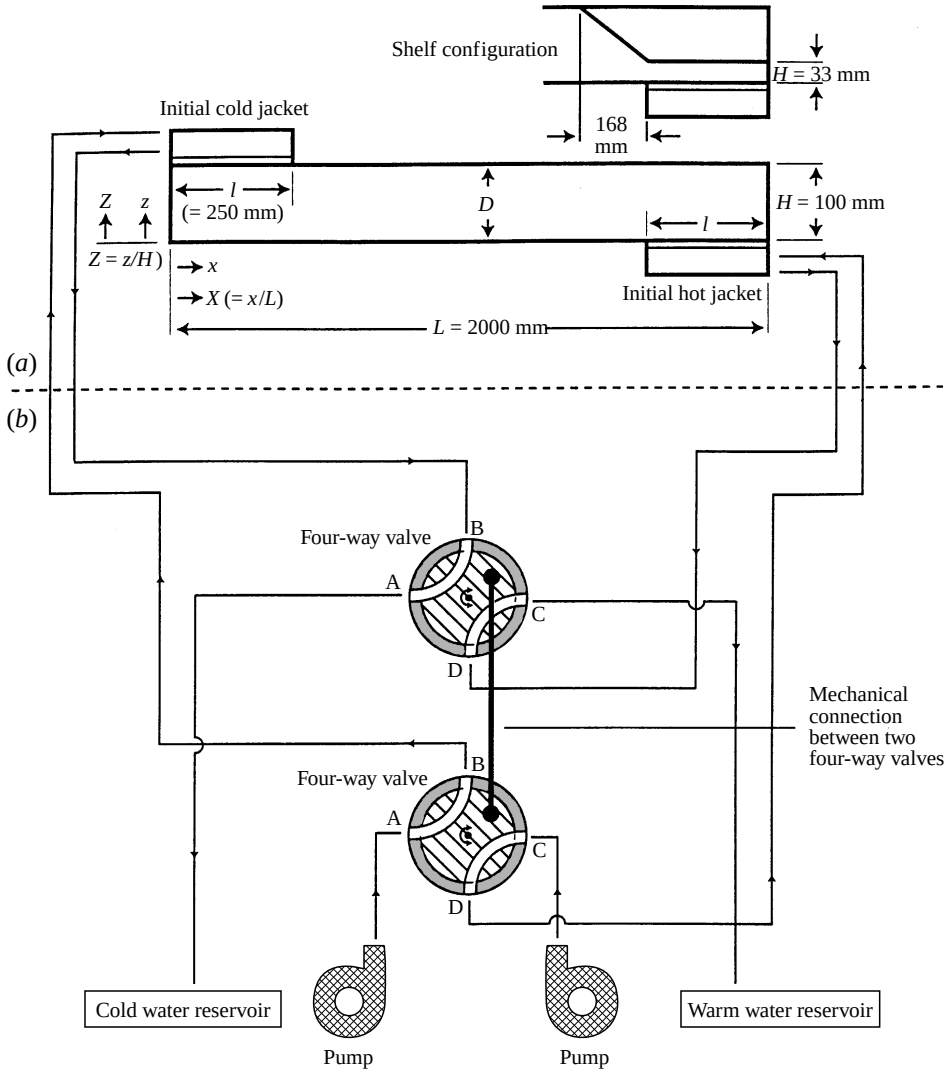

FIGURE 1. (*a*) Schematic diagram of tank, not to scale, with definition of axes. Tank dimension into page: 500 mm. Buoyancy fluxes at ends can be switched in sign by switching hot and cold water flow through the jackets. (*b*) When the channels in the linked four-way valves provide passages connecting AD and BC, warm and cold water are then delivered respectively to the previously cold and warm ends of the tank, thus changing the sign of the buoyancy fluxes.

thermometer. As can be seen in figure 2, though the absolute value of the buoyancy flux was significantly reduced when the forcing was switched from destabilizing to stabilizing, it remained of the same order of magnitude. The difference between the size of the heat fluxes in the two cases of forcing is a consequence of the boundary conditions being prescribed temperatures.

Temperatures within the tank were measured by rapid-response thermistor traverses, of 1 s duration from tank top to bottom, taking 50 samples per traverse. Calibration of these thermistors was also made against a platinum resistance thermometer resulting in an accuracy better than 0.01 °C. Velocities were measured using a particle image velocimetry (PIV) method (see Stevens & Coates 1994) with a vertical light sheet from a 4 W argon ion laser illuminating fluorescent particles of about 100 μm diameter with

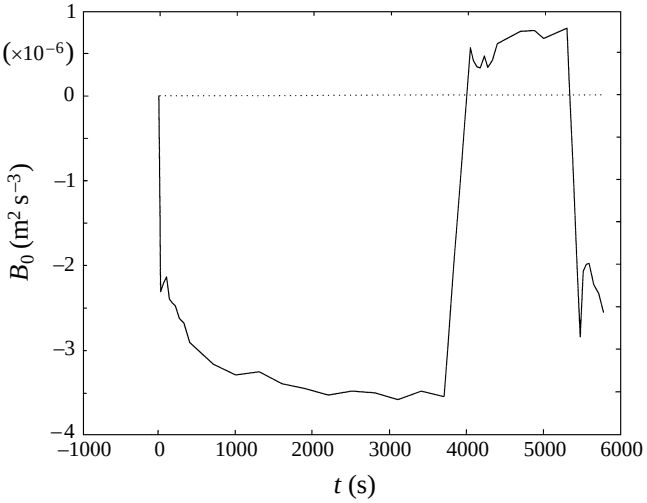

FIGURE 2. A typical example of the experimental forcing buoyancy flux from startup with destabilizing forcing, through a switch to stabilizing forcing and back to destabilizing forcing again. The first point to the right of startup occurs 23 s later.

Experiment number	Time to switch (s)	Configuration	Aspect ratio H/l
3	No switch	Rectangular	1/1
11	2400	Rectangular	1/2.5
15	80	Rectangular	1/2.5
16	400	Rectangular	1/2.5
17 (a, b)	4000	Rectangular	1/2.5
22	1140	Shelf/slope	33/250
23	400	Shelf/slope	33/250
24	80	Shelf/slope	33/250

TABLE 1. Experiment numbers, switching times at which the initial destabilizing forcing is switched to stabilizing forcing, topographical configuration, and aspect ratios of the forcing region. Note that experiment 3 represents data of Sturman *et al.* (1996), with $Ra = 5 \times 10^9$ using the definition of Rayleigh number of this paper. The notation experiments 17a and 17b refers to independent acquisitions of data from the video records of experiment 17.

which the water was seeded. Further details of both velocity and temperature measurements are available in Sturman *et al.* (1996). Heat losses from the tank were approximately 1% of the end to end fluxes.

Two geometrical configurations of the tank have been employed in the current series of experiments. The rectangular tank as described constituted the first configuration, while the second configuration consists of the tank as described but with Perspex inserts located in the end regions to give a shelf of the same length as the forcing plates and a gap of 33 mm between plate and shelf, with the shelf region extending into the tank via a slope terminating at the horizontal tank wall 168 mm from the shelf edge (see the inset sketch in figure 1).

All experiments were conducted at essentially the same Rayleigh numbers. The Rayleigh number was defined as

$$Ra = Bl^4/(\nu\kappa)^{3/2}, \tag{1}$$

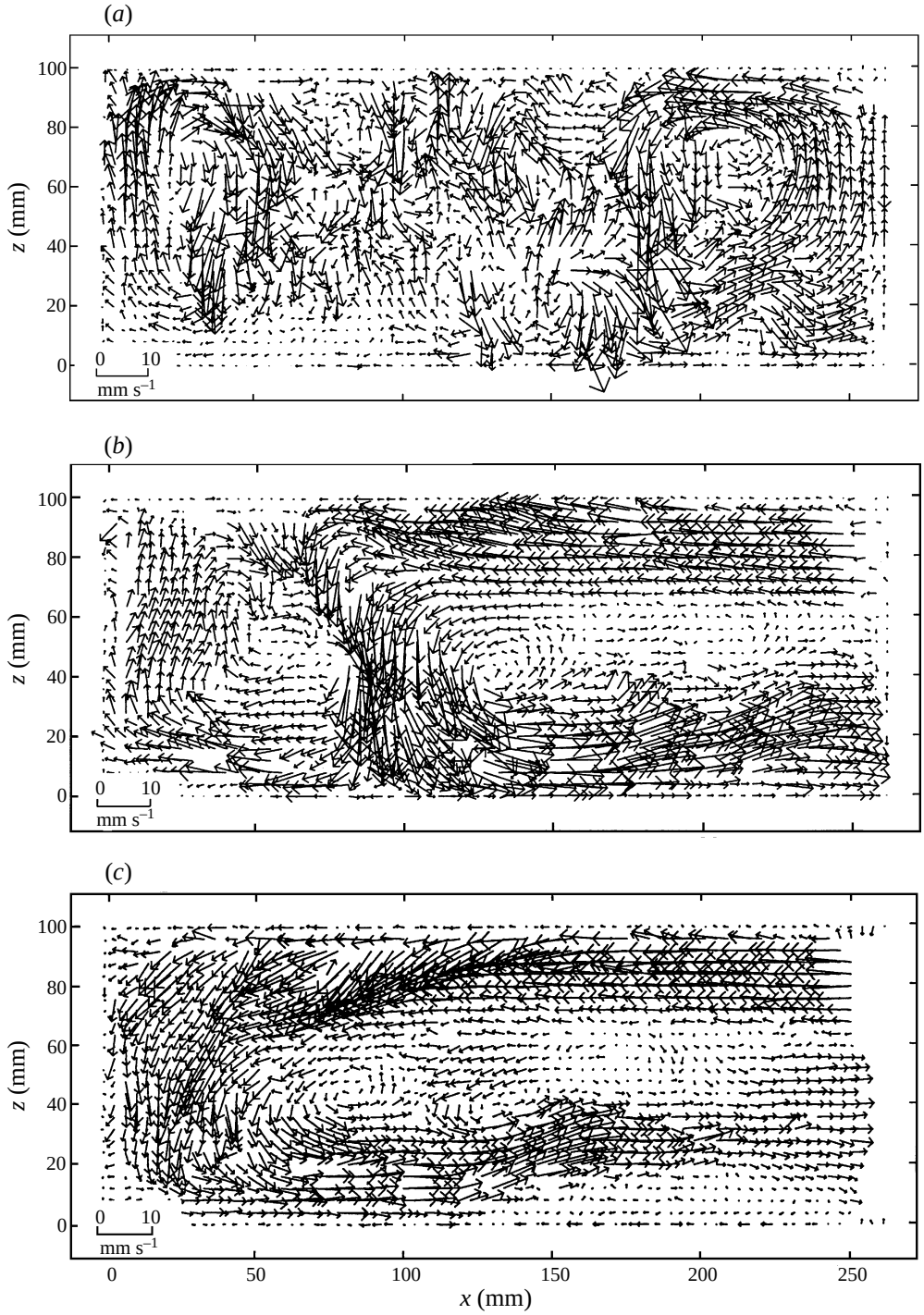

FIGURE 3. Velocity vector maps in the forcing region of the tank, with destabilizing forcing from above in the rectangular tank configuration, experiment 11: (*a*) 45 s, (*b*) 105 s, (*c*) 2385 s after thermal start. The 250 mm mark represents the interior edge of the forcing region.

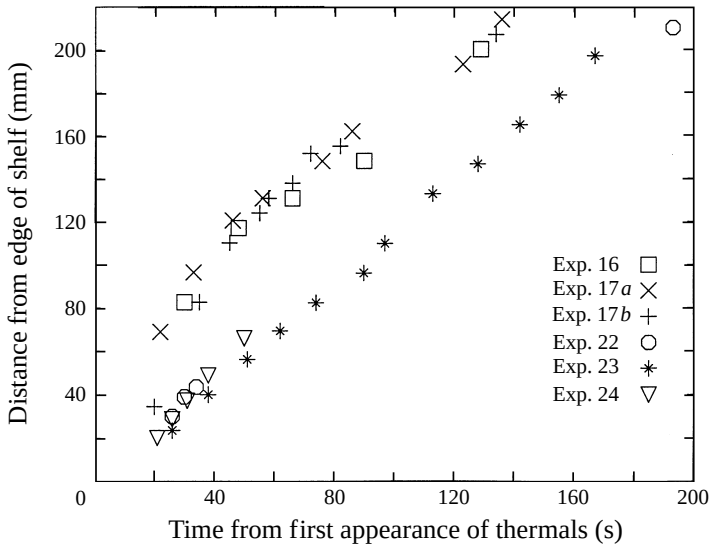

FIGURE 4. Distance of erosion front from leading edge of forcing plate against time from the first visible formation of thermals for both rectangular tank configured experiments (experiments 16, 17*a*, 17*b*) and shelf-slope configured experiments (experiments 22, 23, 24).

where ν and κ are the molecular momentum and thermal diffusivities respectively. In the case of the run in figure 2, for example, prior to the switch at 3700 s and with destabilizing forcing, the Rayleigh number was approximately 2.6×10^{11}. With stabilizing forcing prior to the switch at 5300 s, the Rayleigh number was approximately 0.60×10^{11}. The timescale at which the external forcing was switched is an important free parameter and experiments were started for each of the two geometries with destabilizing forcing and followed by a switch to stabilizing forcing after times of typically 80 s, 400 s and 1140 s or more. The stabilizing forcing was retained for 1440 s in all cases. Table 1 gives more details of the experimental runs and this choice of timescales is discussed below in §5.

3. Experimental results

In the first two subsections we focus on the rectangular tank with no topographic modifications. Section 3.1 describes the end region flows and §3.2 the interior response. The effect of varying the geometry to the shelf configuration in figure 1 is discussed in §3.3.

3.1. *Rectangular configuration – end region* (*forcing region*)

Figure 3(*a–c*) shows the development of the flow under the cold plate for a typical run (experiment 11) with destabilizing forcing, at times 45 s, 105 s and 2385 s, respectively, after thermal start. Following startup, the thermal boundary layer quickly reached the critical Rayleigh number on the forcing surface whereupon thermals formed and they had just reached the bottom boundary or wall in figure 3(*a*), filling the entire end region with turbulent flow. Due to the buoyancy anomaly g' which developed between this end region and the passive interior of the tank horizontal counterflows were established and figure 3(*b*) shows the counterflows and the front (at approximately 80 mm) between the counterflow and the turbulence-dominated regions. The turbulent region was progressively eroded by this mean flow until the front approached the endwall, as shown in figure 3(*c*), which is typical of the end region flow at times after the front's

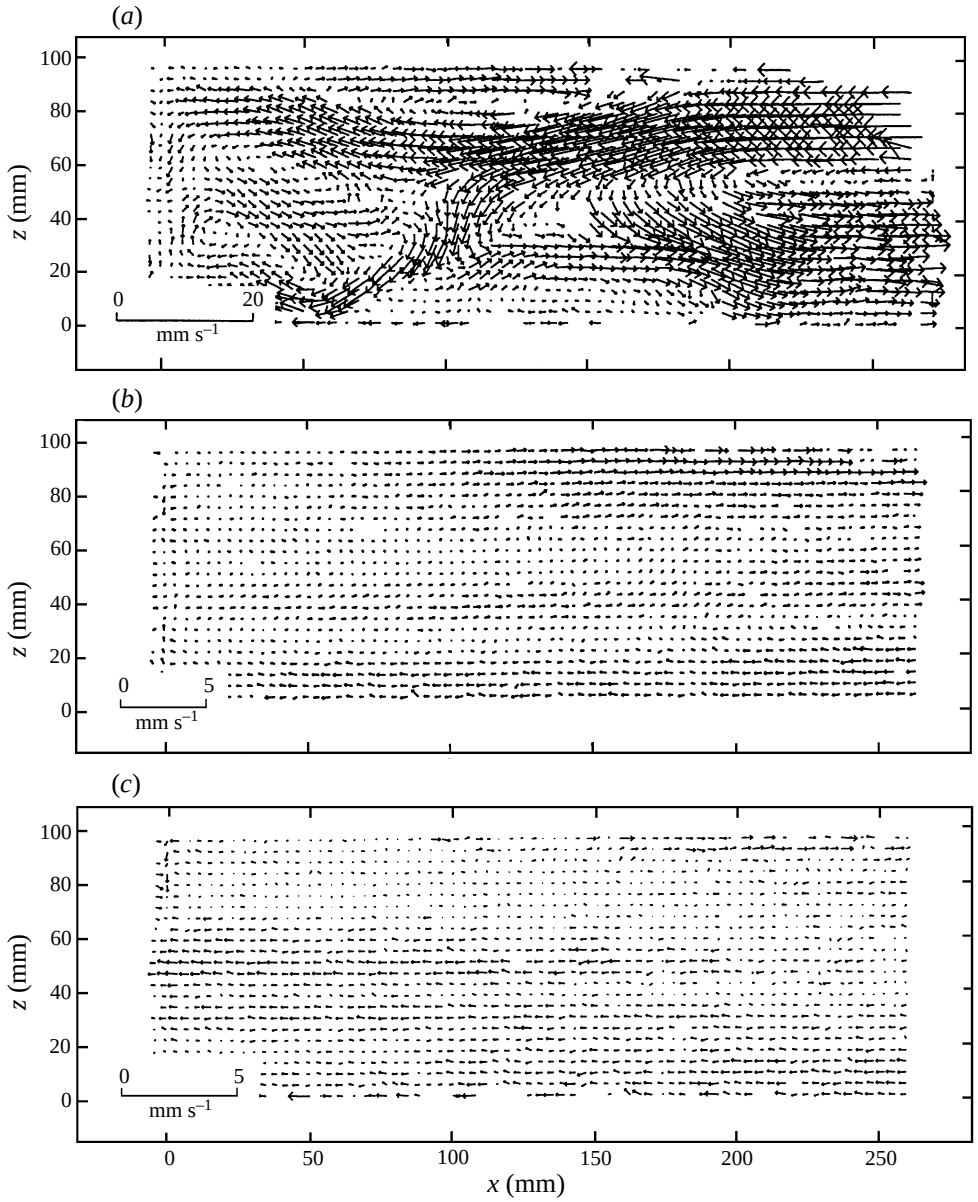

FIGURE 5. Velocity vector maps in the forcing region of the tank, with stabilizing forcing following a switch from destabilizing forcing: (*a*) 40 s, (*b*) 420 s, (*c*) 1020 s after the switch.

arrival near the endwall. A separation feature is evident on the lower wall in figure 3(*c*) between approximately 130 and 250 mm, corresponding with that discussed in Sturman *et al.* (1996). Its location here, within the region of forcing (by contrast with its location external to the forcing region in Sturman *et al.* 1996, but at a similar distance scaled by H from the endwall) suggests that it is a consequence of geometry, rather than of thermal boundary conditions, and in this sense is to be distinguished from the apparently similar separation feature described in Patterson & Armfield (1990), where thermal boundary conditions were central to the formation of the feature they described. The rate of advance of the front separating the counterflow region from

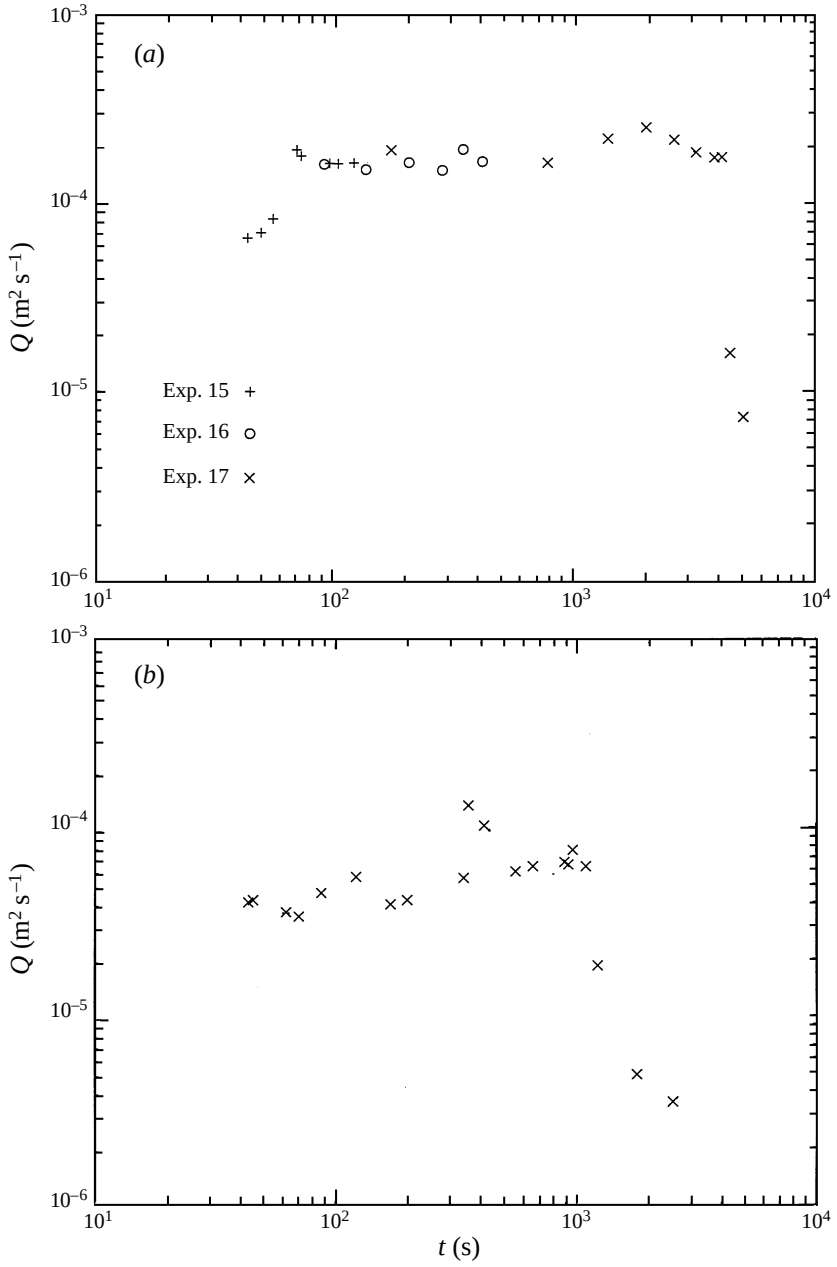

FIGURE 6. Discharge Q from the forcing region against time from thermal start. (*a*) The rectangular tank configured experiments 15, 16, 17 – the switch was at 4060 s after thermal start. (*b*) The shelf/slope configured experiment 22 – the switch was at 1000 s after thermal start.

the fully turbulent region is shown in figure 4, where for the moment we concentrate simply upon the data for experiments 16 and 17. At times greater than about 40 s the penetration of the front appears linearly dependent upon time measured from the appearance of the first thermals, while at earlier times there is a starting adjustment region.

After the initially destabilizing forcing was maintained for 4000 s, the flow was switched to stabilizing forcing: figure 5(*a–c*) displays the subsequent evolution of flow

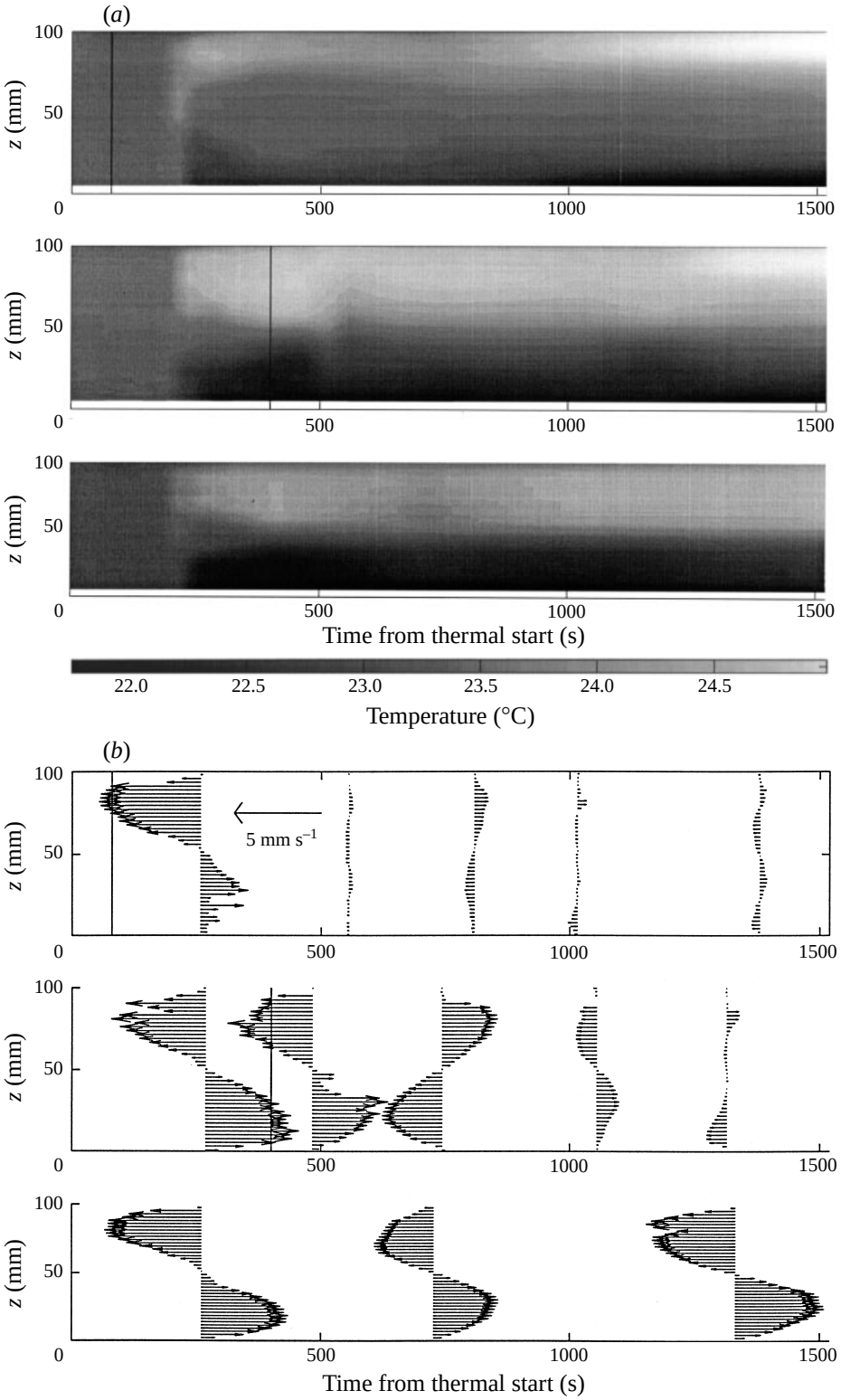

FIGURE 7. For caption see facing page.

at 45 s, 440 s and 1040 s respectively after the switch. In response to this switch, the establishment of a laminar layer flowing in the opposite direction to the mean flow established on the previous destabilizing cycle can be seen at $z = 100$ mm and $50 < x < 140$ mm in figure 5(*a*), while the residual mean circulation from the previous forcing persisted in weakened form near the endwall. The laminar flow hugging the upper wall was clearly established in figure 5(*b*) (note the change of velocity scale) and, interestingly, later in figure 5(*c*) it seems diminished in magnitude and in thickness below the heating surface. Figure 5(*a–c*) implies that the mean flow from the previous regime of forcing retreated to the interior (*z*-direction), while still influencing the present intrusions. Augmentation or retardation of the intrusions in figures 5(*b*, *c*) depended on the phase of cavity-scale residual internal waves which were clearly evident in the video records.

The discharge inferred from figure 5(*c*) when stabilizing forcing was established is very small compared with the corresponding discharge with destabilizing forcing in figure 3(*c*). In order to obtain quantitative discharges from the end regions a polynomial was fitted to the velocity profile near the end of the plate ($x = 250$ mm in figures like figure 3*c*) with the velocity at each row of vectors averaged over six adjacent columns. This polynomial was integrated from the walls to the zero-velocity crossover point and the average of the two resulting discharges was taken. The outcome of this process is shown in figure 6(*a*), where the discharges of experiments 15, 16 and 17 (rectangular configuration) are plotted against time. Discharges after the switch of the sign of buoyancy flux are only included for experiment 17 (the switching time for experiment 17 is 4000 s) so as not to clutter the plot. The dramatic drop in discharge after the switch is evident and its size is decreased by more than an order of magnitude, even though it has clearly not reached steady state after the switch. A constant discharge with destabilizing forcing was attained approximately 70 s after the start of the experiment. Figure 6(*b*) is discussed in §3.3.

3.2. *Rectangular configuration – interior response*

3.2.1. *Overview*

In figure 7 we show three time records, each of velocity and temperature, over the depth of the tank for three different conditions of switching. Switching was undertaken at 80 s, 400 s and 4000 s after the destabilizing start, although here we confine ourselves to the former two switches, simply noting the pre-switch evolution of the flow in the case of the latter experiment. Temperature as a function of z vs. time plotted at $x = 1000$ mm (i.e. the tank centre) is shown in figure 7(*a*), with the three panels from top to bottom corresponding to experiments with the switching times indicated above. Similarly, figure 7(*b*) shows profiles of velocity as a function of z at $x = 1000$ mm, with the times of switching shown on the upper two panels by the vertical solid lines. Velocity and temperature profiles in figure 7(*a*, *b*) are taken at the centre of the tank since the profiles are not functions of x in the interior. The panels are scaled so that figure 7(*b*) corresponds exactly with figure 7(*a*).

The velocity profiles at approximately 1300 s in the top and bottom panels of figure

FIGURE 7. Rectangular configuration of the tank, experiments 15, 16 and 17 represented from top to bottom. (*a*) Temperature profiles over the *z*-domain [5,100] mm at the tank centre ($x = 1000$ mm) against time from thermal start. The greyscale-bar gives the temperature code. (*b*) Horizontal component of velocity u over the height of the tank against time from thermal start. The times at which forcing is switched from destabilizing to stabilizing are represented by the vertical solid lines (80 s in the top panels and 400 s in the middle panels). Note that the panels are scaled so that (*b*) corresponds exactly with (*a*).

7(*b*) represent the closest approximations to steady-state profiles with stabilizing and destabilizing forcing, respectively. While the profile in the bottom panel of figure 7(*b*) displays essentially a cubic profile occupying the full depth of the tank (cf. Sturman *et al*. 1996), the top panel shows a four-layer structure of the velocity profile. The velocities at the very top of the tank are unavailable in figure 7(*b*) with stabilizing forcing because of the downward deflection of the laser light entering the end of the tank due to strong refractive index effects in the laminar boundary layer below the cold plate. Even so, it is evident from the velocity profile in the top panel that the intrusions deriving from stabilizing forcing each occupy about 0.2 H, in contrast to the intrusions deriving from destabilizing buoyancy in the bottom panel which each occupy 0.5 H. Note also that the magnitudes of the velocities in the top panel have decreased by an order of magnitude compared with those in the bottom panel. The tank is already stratified from the previous destabilizing forcing when the buoyancy flux is switched to the stabilizing mode, and the new intrusions act to increase the stratification (see figure 7*a*, top and middle panels). This implies that the stabilizing intrusions should be accompanied by a return flow satisfying continuity in each of the upper and lower halves of the tank.

All three temperature profile panels (figure 7*a*) show that the initial intrusion layers reach the centre of the tank at the same time, approximately 200 s, even with the very short period (80 s) of destabilizing forcing in the top panel. (The mean tank temperature in the lower panel of figure 7(*a*) is displaced from that in the other two panels by about 0.5 C, thus giving it a slightly darker range of greys.) In figure 7(*b*), all three velocity profiles, at approximately 260 s, are essentially the same, surprisingly for the upper panel where the forcing giving rise to the intrusions has been switched in sign at 80 s, dramatically demonstrating how important inertia can be in these flows. The ragged nature of portions of the profiles in the upper two velocity panels for the first 500 s is due to the incomplete mixing of the particles used for seeding for PIV at this relatively early stage of the flow development. The 'pip' in the velocity profile in the bottom frame of figure 7(*b*) at approximately 1300 s is due to a residual eddy from a withdrawn thermistor probe.

3.2.2. *Detailed discussion*

The central panels of figures 7(*a*) and 7(*b*) contain the most noteworthy material, which we will take as our starting point for detailed further discussion.

The centre panel of figure 7(*a*) shows the thermal signature when destabilizing forcing is switched to stabilizing at 400 s. Following the switch, the original intrusion temperature signatures persist remarkably, until the intrusions deriving from the stabilizing forcing arrive at 1200 s. The persistence of the original intrusion temperature signatures up to this time suggests strongly that horizontal advection from the original forcing dominates over the vertical diffusion of heat, at least over the period of time until the new stably derived intrusions arrive. At about 600 s there is a reduction and rise in the temperatures of the upper and lower intrusions, respectively. This occurs because after the startup of the experiment, water from the interior of the tank (at the initial tank temperature) was heated (or cooled) by the plates and discharged as the intrusion layers which finally crossed the centre of the tank, where the temperatures were measured. The intrusions then proceeded to the plate at the opposite end of the tank, where for the first time chilled water arrived over the hot plate and vice versa. When this fluid left the end region it did so at a lower (or higher) temperature than before, and this is reflected in the temperature measurements after the intrusion has turned at the end and traversed a further half of the tank length. The time between an

intrusion first passing the tank centre and the corresponding reduction (or increase) of the intrusion temperature is thus a measure of the time taken for the intrusions to travel one tank length, i.e. about 300 s from the centre panel. The temperature signature of the stably forced intrusion, which first arrives at about 1200 s, is about 20 mm in thickness, about the same as the velocity records. The slight reduction in temperature at the top of the tank ($z = 100$ mm) is due to evaporation from the thermistor access ports.

The middle panel of the velocity records, with the switch at 400 s, gives striking confirmation of the existence of internal waves in the stratified environment, with a complete reversal in direction of the velocity profile between 500 s and 750 s. The internal waves are initiated soon after startup of the destabilizing forcing and are associated with the intrusions reaching the opposite ends of the tank (see Sturman *et al*. 1996). At about 1100 s the velocity profile reverted to its original direction but was considerably attenuated in amplitude. An order of magnitude estimate of the buoyancy frequency resulted in a value of the seiche period of $\tau_s \sim 400$ s. We calculated the buoyancy frequency N in two ways, one for a linear stratification and the other for two distinct layers, where the layers have differing densities from each other but are of uniform density within each layer (see Fischer *et al*. 1979 for the details for the calculation for each case). The stratification in the interior region of our experiments was between the linear case and the two-layer case, consequently we took the geometric mean of the two values of N. From the panel the seiche period is roughly 1100–500 = 600 s, which compares favourably with the order of magnitude estimate. (The video record confirmed that the lower panel did not contain two or more periods of a seiching.) At 1300 s the intrusion from the stabilizing forcing had passed the tank centre and dominated the velocity profile.

The top temperature panel in figure 7(*a*) represents a very short burst of destabilizing forcing of 80 s duration before the switch. Nevertheless the intrusion deriving from this short burst of forcing, delayed in time by approximately 200 s before reaching the centre of the tank, still retained a significant though weaker temperature signature than for the case of the 400 s switch. Note that the hot intrusion arrived just before the cold (see also Sturman *et al*. 1996 where this was noted too). The strength of the temperature signature slowly decayed, until the intrusions from the stabilizing forcing initiated at 80 s arrived at the centre at approximately 900 s. The temperatures of the two intrusions were higher (and lower) than for the destabilizing case, due to the longer residence time of the relatively thin boundary layer over the plate.

In the top panel of figure 7(*b*) the reversal of the velocity profile is evident at about 800 s, though at a much reduced amplitude. At just over 1000 s the bottom intrusion from the stabilizing forcing is evident (the top one not being evident due to refractive index effects noted earlier), with virtually zero velocity in the interior. Yet by nearly 1400 s a non-zero velocity profile has reappeared over approximately $20 < z < 80$ mm, suggesting again the truncated remnants of a seiche. Both the velocity profiles of the stably forced intrusions and their thermal signatures extend over approximately $0 \leqslant z \leqslant 20$ mm and $80 \leqslant z \leqslant 100$ mm.

Finally in the bottom panel of figure 7(*a*), we see the thermal signature of the unstably derived intrusions without any switching. Internal waves are also implied from the bottom panel of figure 7(*b*), where the magnitude of the velocities is lower, about 30 % less at 700 s than at 250 s and 1300 s, but there is nothing as dramatic as the reversal of directions of the velocities seen in the upper two panels. We conclude that the switch of the buoyancy flux sign at the end regions and its timing has a large impact upon the strength of the tank-scale internal waves.

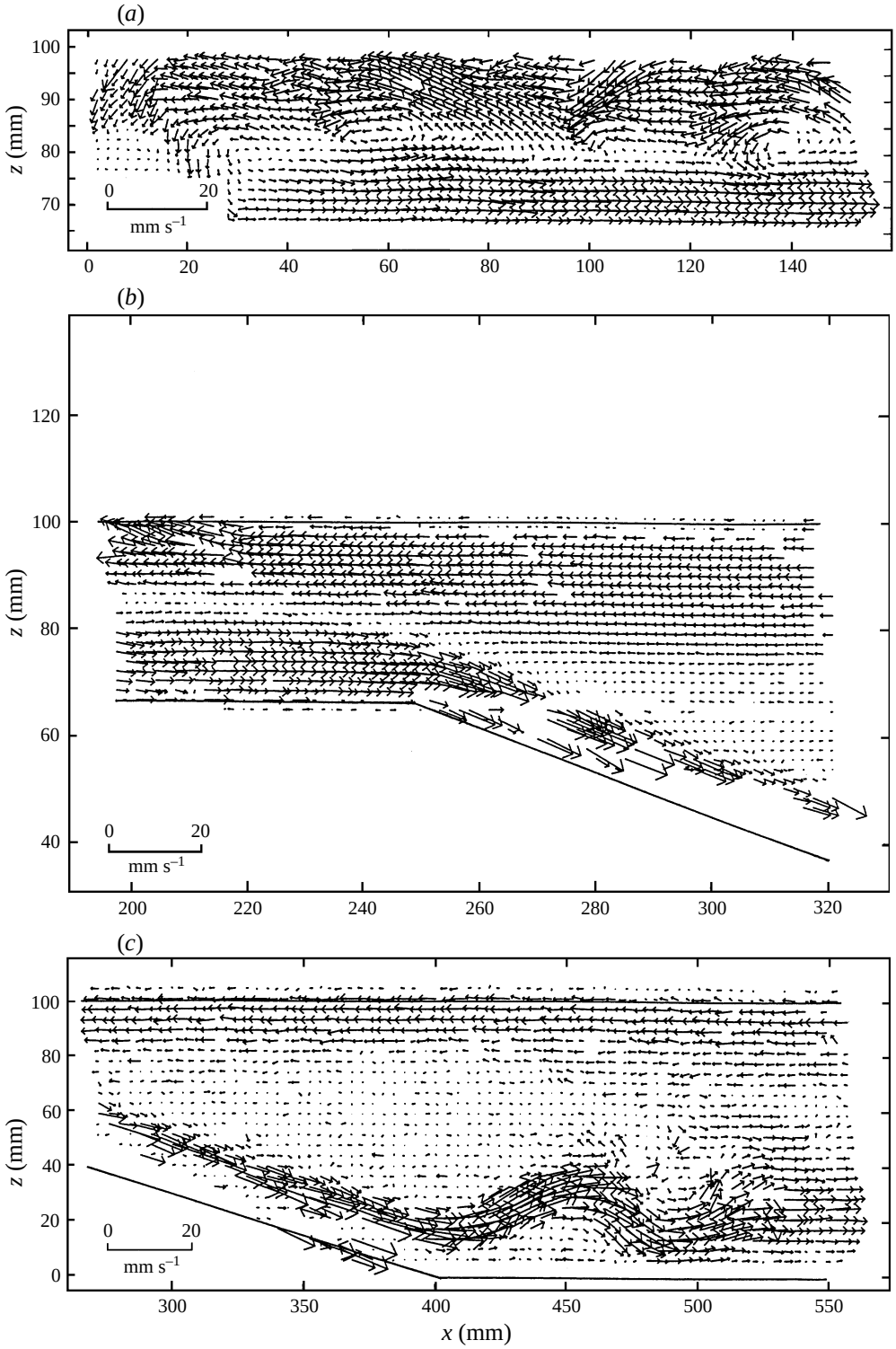

FIGURE 8. Velocity vector maps in the forcing region of the tank, with destabilizing forcing from above in the shelf/slope configuration, experiment 22: (*a*) tank end at 630 s, (*b*) shelf/slope breakpoint at 670 s, (*c*) shelf/floor breakpoint at 515 s, all times after thermal start.

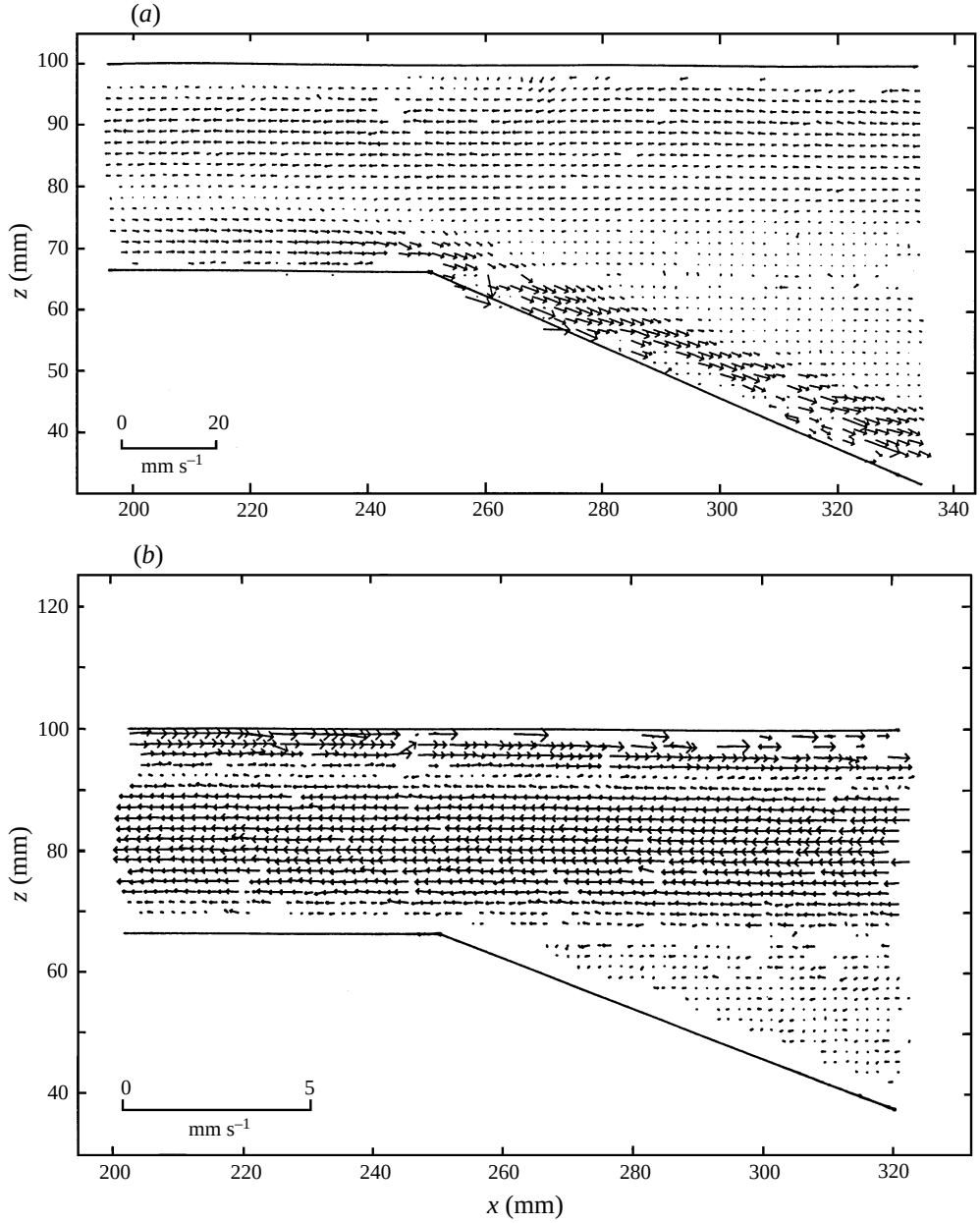

FIGURE 9. Velocity vector maps in the forcing region of the tank, with stabilizing forcing from above in the shelf/slope configuration at the shelf/slope breakpoint, experiment 22 at: (*a*) 100 s, (*b*) 660 s, all times after switch.

3.3. *Shelf configuration*

3.3.1. *Experimental results*

The major difference from the earlier configuration is that in the shelf configuration the depth of the fluid in the forcing region is much smaller, with the ratio of the shelf depth to forcing length now 33/250.

Erosion of the fully turbulent region by the mean flow is shown in figure 4, runs 22,

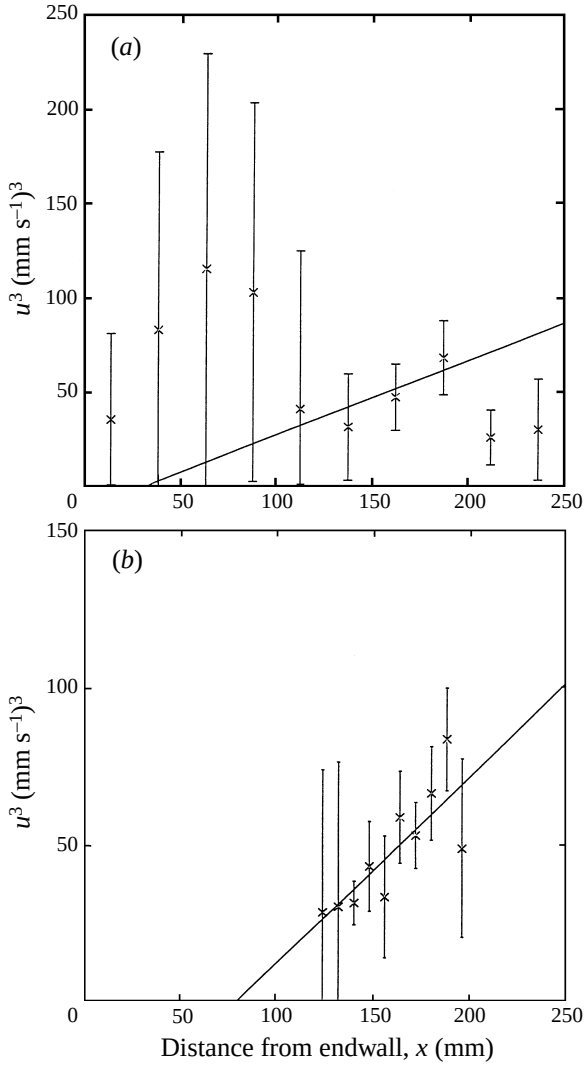

FIGURE 10. (*a*) Ensemble mean horizontal velocity components u^3 near the forcing plate surface against distance from the tank endwall over the whole plate length. The solid line is Phillips' (1966) scaling as fitted to the data in (*b*). (*b*) The data are plotted in the same manner as (*a*) but only over the domain $120 \leqslant x \leqslant 200$ mm and the solid line is the least-squares fit of Phillips' scaling.

23 and 24. Note that the progress of the erosion front, like that in the rectangular box, was linear over most of the time domain, except for small times. When the discharge flow had fully flushed the forcing region it showed considerable differences from the earlier rectangular arrangement and a representative selection of velocity vector maps derived from the PIV process is shown in figure 8(*a–c*).

Figure 8(*a*) shows the cavity flow from the tank endwall to just over halfway along the plate, with destabilizing forcing. Where the shelf changes to a slope is the next region of interest and in figure 8(*b*) we see that the inflow has contracted and accelerated as it was squeezed to about half the shelf depth and then, at about 220 mm, the effects of convective cooling can be seen locally disturbing the inflow. In contrast, the lower return flow accelerated as it left the shelf and descended down the slope. The

quality of the figure is impaired here because of the very large shear distorting the rectangular windows upon which the PIV process is based and due to glare from the laser light on the slope. An attempt to minimize this effect by subtracting a background image integrated over a long period from the selected images for the PIV process was not successful in this case. Even so it is clear that there was a fairly well-defined high-speed stream descending the slope. When this stream reached the bottom of the slope (see figure 8*c*) it separated from the tank bottom producing a standing-wave-like structure, until finally it moved into the tank interior as an essentially parallel flow of much greater thickness than the stream descending the slope. This region has the appearance of an internal 'hydraulic' jump (see further §5 below).

When the sign of the forcing buoyancy flux has been switched, the residual flow continues to dominate the end region at 100 s after the switch, see figure 9(*a*), although the magnitudes of the velocities are much reduced. On the plate itself (see upper boundary to 250 mm) the velocity is very small and the downflow at 270 mm suggests the start of a laminar counterflow to the right along the plate, though this is not yet reflected by the velocity vectors adjacent to the plate. A laminar boundary layer and intrusion was well established by 660 s after the switch, see figure 9(*b*), with no residual flow down the slope.

Comparisons and contrasts between the discharges from the rectangular-configured forcing region and the shelf-configured counterpart are possible using figures 6(*a*) and 6(*b*). The uppermost two points in figure 6(*b*) for experiment 22 (shelf/slope configuration) have captured the passage of the intrusion layer derived from the opposite end of the tank as it passed the leading edge of the forcing plate, with a spike of increased discharge. Records of the discharge following the switch persist considerably longer than in figure 6(*a*), and suggest a final discharge with stable forcing of between 1×10^{-6} and 3×10^{-6} m^2 s^{-1}, about 1/30th of the magnitude of the discharge from destabilizing forcing. As the discharge from the stabilizing forcing is expected to be the same in both of the configurations (see §4.1.2) the discharge from stabilizing forcing is estimated to be two orders of magnitude less than the discharge from destabilizing forcing for the rectangular configuration too. Note also that the discharge from destabilizing forcing in the rectangular configuration is about three times that in the shelf/slope case. Because H in the rectangular case is three times that in the shelf/slope case, the ratio of discharges suggests the discharge scales as H.

4. Analysis

4.1. *Scaling*

4.1.1. *Destabilizing forcing*

In laboratory experiments with the aspect ratio of forcing $H/l = 1$ and no sill, Sturman *et al.* (1996) found that the scaling of Phillips (1966) applied globally, i.e. $u \sim (Bl)^{1/3}$. We now attempt to test it locally, that is to answer the question: is $u \sim (Bx)^{1/3}$?

Figure 10(*a*) shows the results of plotting the horizontal components of local velocities against distance from the tank endwall in the present experiments with $H/l = 0.13$. Approximately 1000 individual velocity vectors were used to construct figure 10(*a*). The velocity magnitudes plotted are ensemble averages and the geometric details of the averaging process will be easier to understand by referring to figure 8(*a*). Each column of velocity vector x-components was averaged over rows 1 to 3 from the top. A five-column running average was then calculated over the x-domain and the

results assigned to ten equal-sized bins into which the x-domain was divided. This process was undertaken on each of five independently acquired velocity vector maps at 'steady state' and at different times for the same experiment, and an ensemble average was formed over corresponding bins within each of the five maps as shown in figure 10(*a*).

From the endwall to say 120 mm, the turbulent fluctuations of velocity are of at least the same order of magnitude as the mean velocity, rendering the data unusable (recall that Phillips' results are for the mean velocity and note that the error bars shown in the figure represent ± 1 standard deviation). The PIV process we use for obtaining velocities is not ideal for obtaining a large sample size of local velocities over time to enable a reasonable average in time to be obtained. Additionally, Phillips (1966) shows that his scaling will not apply within distance $O(H)$ from the endwall. From 120 mm to about 200 mm is a region where the turbulent fluctuations are more moderate by comparison with the mean velocity, and the data are more reliable. From 200 mm to the leading edge of the forcing plate the data have a similar standard deviation to those between 120 mm and 200 mm, yet are low in value. As mentioned above, in order to improve the quality of the velocity data we have averaged the x-component of the three rows of velocity vectors immediately adjacent to the thermal forcing plate at each column of vectors. Doing this exacts a price. The three rows near the leading edge of the plate are not all within the forcing boundary layer, but some reflect instead the velocities of the laminar boundary layer on the start of the plate (see Sturman *et al.* 1996) and of the return flow from the far end of the tank. Thus we expect that the velocities near the leading edge of the plate will not be predicted by Phillips' (1966) result. The line in figure 10(*a*) is a least-squares fit with low credibility on the data only in the domain $120 \leqslant x \leqslant 200$ mm. We assume that data in this domain alone are of sufficient quality to warrant a test of scaling, but clearly the binned data in figure 10(*a*) are too sparse. In constructing figure 10(*b*) we returned to the original raw velocity data in this domain only, assigned the averaged velocity to ten bins and ensemble averaged as before. (We used approximately 350 individual velocity vectors.) The least-squares fit implies the reasonableness of Phillips' scaling, but is not unequivocal support as the slope of the line, and hence the virtual origin inferred by the intersection of the fitted line with the x-axis, is not sharply defined due to the relatively large standard deviations of the data and the very small useable range of x. A similar least-squares fit over the same range of data in figure 10(*a*), but giving a factor of 2 difference in the virtual origin, underlines this point. A very long forcing plate, together with measurement and averaging of a sizeable sample of local velocities over time will be required in future experiments to understand better the variation of u with x.

We conclude from figure 10(*b*) that the local scaling of Phillips (1966), i.e. $u \sim (Bx)^{1/3}$, is not inconsistent with the data. (Note too that we have not presented a similar plot for the case of $H/l = 0.4$ as entry and endwall effects occupy too great a proportion of the x-domain to allow any meaningful results.) Certainly globally it is consistent (e.g. Sturman *et al.* 1996) and clearly a larger facility than the present one is required to obtain more definitive testing. We note, however, that the location of the virtual origin inferred in figure 10(*b*) (and 10*a*) is consistent with the hypothesis that the virtual origin is of $O(H)$ distant from the endwall.

The discharge initiated by destabilizing forcing Q_- will be given by $Q_- \sim uH$ at 'steady state' as H is the scale over which discharge occurs. Thus using (1)

$$Q_- \sim (B_- l)^{1/3} H \sim Ra_-^{1/3}\, Pr^{1/2} (H/l)\, \kappa, \tag{2}$$

and (2) is valid provided $H/l < O(1)$.

4.1.2. *Stabilizing forcing*

When the buoyancy flux is stabilizing, at steady state the laminar conduction of heat into the fluid is balanced by horizontal convection of heat:

$$u\frac{\partial T}{\partial x} \sim \kappa\frac{\partial^2 T}{\partial z^2}. \tag{3}$$

Given that x scales as l, the forcing plate length, and that z scales as δ, the boundary layer thickness, then introducing these scales into (3) gives rise to

$$u \sim \kappa l/\delta^2. \tag{4}$$

Assume that inertia and viscosity are both important (see below) and that there is a three-way balance between these terms and buoyancy at steady state. The momentum equation becomes

$$\frac{\partial}{\partial z}\left(u\frac{\partial u}{\partial x}\right) \sim \nu\frac{\partial^3 u}{\partial z^3} + g\alpha\frac{\partial T}{\partial x} \sim \nu\frac{\partial^3 u}{\partial z^3} + \frac{\partial g'}{\partial x}, \tag{5}$$

where $g' = g(\Delta\rho/\rho) = g\alpha\,\Delta T$ is a measure of the buoyancy anomaly between the fluid in the boundary layer on the plate and the ambient fluid. Note that the order of magnitude of the heat flux conducting into the fluid is $F_H \sim k\,\partial T/\partial z \sim k\Delta T/\delta$, where ΔT is the temperature difference across the boundary layer, the thermal conductivity k is related to the thermal diffusivity κ by $k = \kappa\rho C_p$ (C_p being the specific heat) and buoyancy flux is defined by $B = F_H\,\alpha g/\rho C_p$ and hence $g' \sim B_+\,\delta/\kappa$, where B_+ is a stabilizing buoyancy flux. Initially take the inertia buoyancy balance in (5). Introducing this expression for g' into (5) together with the appropriate scales and eliminating u between (4) and (5) leads to

$$\delta_I \sim \kappa^{1/2} l^{1/3}/B_+^{1/6}. \tag{6}$$

Substitution of (6) into (4) and making use of the definition of Ra in (1) gives rise to

$$u_I \sim (B_+ l)^{1/3} \sim Ra_+^{1/3}\,Pr^{1/2}\kappa/l. \tag{7}$$

Hence using (6) and (7) the volume discharge with stabilizing buoyancy flux and an inertia buoyancy balance, $Q_{+I} \sim u\delta$, is given by

$$Q_{+I} \sim (B_+ l)^{1/3}\delta_I \sim Ra_+^{1/6}\nu/Pr^{3/4}. \tag{8a}$$

If a viscous buoyancy balance is taken in (5) the corresponding result for discharge is given by

$$Q_{+V} \sim (B_+ l)^{1/3}\delta_V/Pr^{1/3} \sim Ra_+^{1/6}\nu/Pr^{11/12}. \tag{8b}$$

From equations (2) and (8*a*):

$$Q_-/Q_{+I} \sim (B_- l)^{1/3}H/(B_+ l)^{1/3}\delta_I \sim (Ra_-^{1/3}/Ra_+^{1/6})\,Pr^{1/4}(H/l). \tag{9}$$

The assumption that there is a three-way balance between viscous, inertia and buoyancy terms in the momentum equation (5) will now be considered. Take the ratio of inertia to viscous terms in (5). For the ratio to be greater than $O(1)$ requires

$$Pr < O(1). \tag{10}$$

We use water with $Pr = 7$ and the two cases will be virtually indistinguishable (compare (8*a*) with (8*b*)). There is indeed a three-way balance.

Evaluating (9) with parameter values for the present experiments ($Ra_+ \approx 0.6\times10^{11}$, $Ra_- \approx 2.6\times10^{11}$, $H/l = 0.4$ (rectangular configuration), $H/l = 0.13$ (shelf/slope)), gives

$Q_-/Q_{+I} \approx 66$ (rectangular) and $Q_-/Q_{+I} \approx 22$ (shelf/slope) (multiply by a factor of $(1/Pr)^{1/6} \approx 0.7$ if the viscous buoyancy balance is used) compared with values for Q_-/Q_+ of 30 and 20, respectively, from experimental results in figures 6(*a*) and 6(*b*). This suggests a coefficient of $O(1)$ in (9), (0.5 and 1 respectively from each of the two points) though the discharges from stabilizing forcing in these figures have not quite reached steady state for which (9) is valid.

4.1.3. *Timescales*

The above derivations apply at steady state, but consider now the situation where the fluid is initially isothermal and quiescent before the destabilizing forcing is initiated.

Although the timescale of the formation of the thermals after initiation of the forcing flux is not of direct relevance in field applications, we include it here for completeness. The boundary layer is unstable when the critical Rayleigh number (based upon the boundary layer thickness and the temperature difference between the forcing plate and the interior) is reached. With an endwall present adjacent to the forcing plate the value of the critical Rayleigh number is 1108 (Turner 1973). The critical time τ_{crit} at which thermals will begin to form because of boundary layer instability is thus given by

$$\tau_{crit} \sim \delta_{crit}^2/\kappa \sim \frac{1}{\kappa^{1/3}}\left(\frac{Ra_{crit}\,\nu}{g'}\right)^{2/3} \sim 21 \text{ s}, \tag{11}$$

which compares with the observed value of 17 s. (Here only, $Ra = g\alpha\,\Delta T\delta^4/\nu\kappa$, where g is acceleration due to gravity, ΔT is half the temperature difference between the forcing plates and δ is the thickness of the thermal boundary layer.) Note that this is of the same order of magnitude as the timescale of the initiating flux, but that the measured timescale is still consistent with the scaling despite the 'ramping' of the starting flux. The vertical velocity scale of the thermals is subsequently given by $w \sim (Bz)^{1/3}$ (e.g. Adrian, Ferreira & Boberg, 1986) and the time taken after formation for them to reach the opposite wall is thus

$$\tau_t \sim H/(BH)^{1/3} \sim H^{2/3}/B^{1/3}. \tag{12}$$

Equation (12) gives $\tau_t \sim 7$ s for the shelf/slope arrangement and $\tau_t \sim 15$ s for the rectangular tank. Corresponding observed values are 10 s and 23 s, respectively, consistent with the prediction in (12).

At this time the whole of the end region of the tank adjacent to the forcing zone is occupied by essentially small-scale three-dimensional convection with no mean flow, with a buoyancy anomaly between it and the interior of the tank. Meanwhile the horizontal buoyancy anomaly causes a mean horizontal flow to be established and intrude into the end region, to turn at a front and to discharge from the region (as defined and described in §3.1). By analogy with equation (2) the discharge from the region of length l_F from the leading edge of the forcing plate to the front is given by

$$Q_- \sim (Bl_F)^{1/3}H. \tag{13}$$

Let the velocity of the front be u_F. Then assuming an inertia–buoyancy balance across the front, l_F is given by

$$l_F \sim u_F\,t \sim (g'H)^{1/2}t, \tag{14}$$

where $g' \sim B^{2/3}/H^{1/3}$ is the buoyancy anomaly between the fully turbulent region and the interior of the tank and H is the thickness scale of the gravity current eroding the fully turbulent region at the front. Equation (14) thus implies $u_F \sim (BH)^{1/3}$ and hence from (13)

$$Q_- \sim B^{4/9}H^{10/9}t^{1/3}, \tag{15}$$

which is valid for

$$t < l/u_F, \tag{16}$$

or

$$t < l/B^{1/3}H^{1/3}, \tag{17}$$

where $l_F \to l$ corresponds to the front approaching the tank endwall. The time associated with this arrival

$$\tau_F \sim l/B^{1/3}H^{1/3} \tag{18}$$

is the forcing-region flushing timescale or 'shelf' flushing timescale. Evaluation of (18) for the shelf/slope configuration and for the rectangular end configuration results in $\tau_F \sim 55$ s and $\tau_F \sim 40$ s, respectively, corresponding to the mean observed values of 210 s and 165 s (see too, figure 4) thus suggesting a coefficient of approximately 4 in equation (18).

Another important timescale, especially in lakes with sidearms, is the filling-box time τ_b, which is defined as the time taken for the fluid in the whole box (tank) to pass once through the boundary layers over the forcing plates, giving a timescale for arrival of the entire flow at 'steady state'. Thus in the case of the rectangular end configuration

$$\tau_b \sim DL/Q_-, \tag{19}$$

where D is the interior depth of the tank, L is the tank length and we have used Q_-.

For intrusions resulting from stabilizing forcing it is somewhat meaningless to define a filling-box timescale, as the whole of the fluid of the tank never passes through a selected boundary layer because stratification confines the return flows to either the top or the bottom half of the tank as long as the tank remains stratified. Nevertheless, the stably derived intrusions do set up an exchange flow as if they were in a one-sided experiment, because the confined flows do not communicate with the forcing plate on the opposite wall of the tank over the timescales for which the experiment was run. If we define the stably forced exchange timescale, τ_E, as the time taken for the total volume of the exchanging fluid (i.e. $2\delta L \sim \delta L$) to pass once through the forcing boundary layer this yields

$$\tau_E \sim \delta L/Q_{+I} \sim \delta L/u\delta \sim lL/\kappa Ra^{1/3}Pr^{1/2}. \tag{20}$$

Equation (20) provides a timescale for the stabilizing flow to reach steady state, approximately 3×10^3 s in the present tank from runs in table 1.

We are now in a position to reflect upon the times in earlier figures in scaled terms. For the rectangular configuration $\tau_F \approx 160$ s and $\tau_b \approx 200$ s. Therefore in figure 3, for example, (*a*), (*b*) and (*c*) correspond to approximately 0.3, 0.6 and 14 end-region flushing timescales and equally to approximately 0.2, 0.6 and 12 filling-box timescales. Thus the figure spans the transient and steady-state regimes for both the end-region flushing and tank flushing timescales.

4.2. *Scaled results*

The flushing of the forcing region is summarized in figure 11, using data from all experiments covering both the rectangular and the shelf/slope configurations. The time t, which appears in both the abscissa and in the ordinate is the time from the first appearance of buoyant plumes associated with the forcing plate. Time in the abscissa is scaled by the flushing time of equation (18). (Note that we include the coefficient 4 so that the abscissa spans a non-dimensional time domain of [0, 1].) The ordinate is scaled by the length of the flushing region from equation (14). Clearly the data for individual runs sometimes cover only a limited timespan. However when all data are

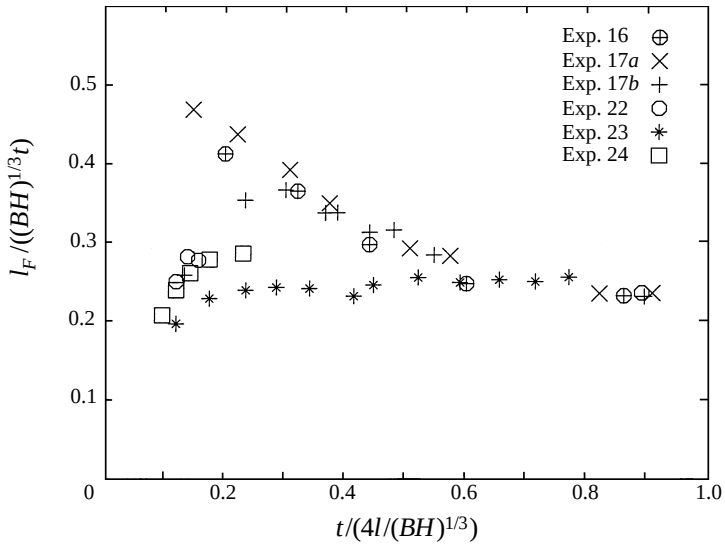

FIGURE 11. Non-dimensional distance of erosion front from forcing-plate leading edge $l' = l_F/\{(BH)^{1/3}t\}$ against non-dimensional time $t' = t/\{4l/(BH)^{1/3}\}$ from experiments 16, 17, 22, 23, 24.

considered together, figure 11 plainly suggests $l' \to 0.25$ after $t' \approx 0.6$. The scaling for l' applies for distance of $O(H)$ or greater from the leading edge. This is possibly due to a combination of several factors: the time taken for the plumes to reach the opposite wall, further transient adjustments when they do, and transient inertial effects which interfere with the simple erosion frontal scaling $u_F \sim (g'z)^{1/2}$ at short times. Additionally there exists a laminar rather than a turbulent boundary layer near the entry region, see Sturman *et al.* (1996). At longer times the scaling collapses well onto a line and suggests

$$l_F = 0.25(BH)^{1/3}t. \tag{21}$$

In the field, where aspect ratios are very small, the starting and entry effects of the laboratory experiment will be wholly unimportant.

Non-dimensional discharges versus non-dimensional time are shown in figure 12 for the shelf/slope and rectangular end regions of the present experiments and also for the earlier experiments of Sturman *et al.* (1996), where $l/H = 1$. The time axis is non-dimensionalized by the filling-box time (see equation (19)), while the discharge axis is scaled by the discharge of equation (2). The velocity scaling $u \sim (BH)^{1/3}$ (see Brocard & Harleman 1980) was also tried but did not collapse the data. The outcome using Phillips' (1966) result was a collapse of all data onto a line at non-dimensional times greater than $O(1)$. Figure 12 suggests an asymptotic approach to

$$Q_- = 0.2(Bl)^{1/3}H, \quad \text{valid for } t_d > 2. \tag{22}$$

4.3. *Summary of timescales and regimes*

As depicted in figure 2, the experiments were forced initially with a negative buoyancy flux for a period τ_- after which the sign of the buoyancy flux was switched and the positive buoyancy flux was sustained for a period τ_+. At $\tau_{crit} \sim \delta_{crit}^2/\kappa$ (equation (11)) the thermal boundary layer has grown to reach the critical thickness at which thermals can start to move from the boundary. From τ_{crit} until $\tau_t \sim H^{2/3}/B^{1/3}$ (equation (12)), thermals proceed to the opposite wall, the region of forcing is progressively filled with turbulence and the regime is characterized by no mean flow. An erosion front begins

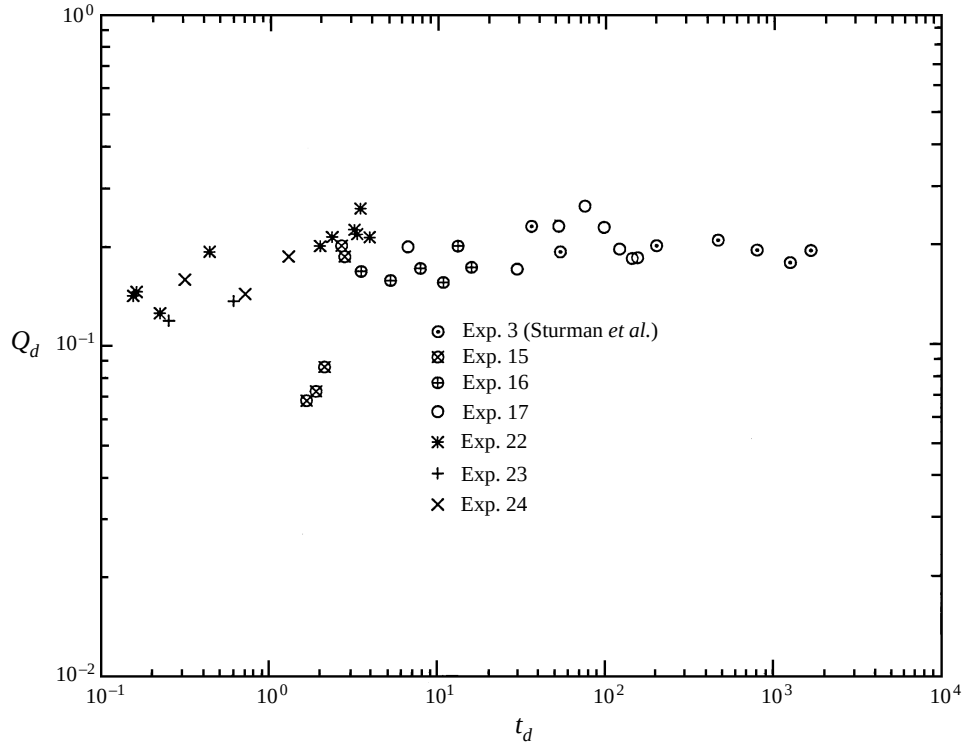

FIGURE 12. Non-dimensional discharge from the forcing region $Q_d = Q_-/(Bl)^{1/3}H$ against non-dimensional time $t_d = t/\{LD/(Bl)^{1/3}H\}$ from experiments 3 (Sturman *et al.* 1996), 15, 16, 17, 22, 23, 24.

to move from the leading edge of the forcing plate towards the endwall, with the front located at a distance l_F from the leading edge. The time taken for the front to approach the endwall of the tank, the forcing region flushing time, is given by $\tau_F \sim l/B^{1/3}H^{1/3}$ (equation (18)). In this regime the portion of the forcing region between the front and the endwall is occupied by turbulent flow, with no exchange between it and the remainder of the tank, while that between the leading edge of the forcing plate and the front has a growing exchange flow with the tank interior of magnitude $Q_- \sim (Bl_F)^{1/3}H$ (equation (13)), increasing with l_F until it approaches l.

A further important timescale associated with this regime in the forcing region is the time taken for the volume of the fluid in the forcing region to be exchanged with the interior, $\tau_{ff} = l_F/(Bl_F)^{1/3}$. Interestingly, this is always smaller than τ_F, provided $H/l < 1$. This means that when l_F approaches l, the whole of the forcing region has already been completely flushed. When $t > \tau_F$, no further obvious regime change occurs in the forcing region, but the tank only approaches steady state when the whole of the fluid in the tank has passed through the boundary layer, that is at $\tau_b \sim DL/Q_-$ (equation (19)), i.e. $\tau_b \sim L/(Bl)^{1/3}$. The condition $\tau_b > \tau_F$ requires that

$$(H/l)^{1/3} > l/L. \tag{23}$$

If (23) is not satisfied, the whole of the tank fluid will have exchanged through the forcing region before the front has reached the endwall. Suppose that $t > \tau_F$ and $t > \tau_b$ and the buoyancy flux is switched so that forcing is now stabilizing. Prior to the establishment of the new steady thermal boundary layer over the plate, and for some further period, the residual flow from the previous destabilizing forcing will persist.

Meanwhile the discharge from the new laminar boundary layer is given by $O_{+I} \sim Ra^{1/6}Pr^{-3/4}\nu$ (equation (8)), with the timescale to steady state given by $\tau_E \sim lL/\kappa Ra^{1/3}Pr^{1/2}$ (equation (20)).

5. Discussion

Møller (1984) has reported some field results which are consistent with the form of (22). The earlier data of Brocard & Harleman (1980) in fact agree with the coefficient in (22), but Møller's own data have a coefficient closer to 0.4. Apart from the issue of the precise value of the coefficient, the experimental results above demonstrate that at steady state the discharge from the convecting region is given by equation (22), which implies that the average discharge velocity is

$$u \sim (Bl)^{1/3}, \tag{24}$$

and that Phillips' (1966) scaling is correct globally, which was our starting point from §4.1.1.

At steady state, conservation of heat for the control volume defined by the convecting or shelf region requires

$$Bl = Qg' \tag{25}$$

and substituting (24) (derived by scaling argument below) into (25) implies that

$$g' = 5\frac{B^{2/3}l^{2/3}}{H} \sim \frac{B^{2/3}}{H^{1/3}}\left(\frac{l}{H}\right)^{2/3}. \tag{26}$$

The coefficient derives from the experimental result (22). Two points are worth noting here. First, in the limit of very short shelves when $l/H \leqslant O(1)$ – the case considered by Sturman *et al.* (1996) – the buoyancy anomaly reduces to $g' \sim B^{2/3}/H^{1/3}$, the known result for the one-dimensional case in vertical Rayleigh–Bénard convection (cf. Adrian *et al.* 1986; Sturman *et al.* 1996). Secondly, the scaled estimates in (24) and (26) taken together represent a simple extension of the suggestion of Phillips (1966) who considered the case where the flow is influenced by the presence of the bottom boundary (in his case a shallow sill of depth H at the entrance to the convecting region of depth greatly in excess of H). We are hypothesizing that the result is valid for a shelf of uniform depth H.

Phillips (1966) suggested that at steady state the momentum balance in the horizontal direction was of the boundary layer form with a three-way balance between the nonlinear terms, the pressure terms and the turbulent terms of the form

$$u\frac{\partial u}{\partial x} + w\frac{\partial u}{\partial z} = \frac{1}{\rho}\frac{\partial p}{\partial z} - \frac{\partial}{\partial z}(\overline{u'w'}). \tag{27}$$

Following Phillips (1966) by assuming the flow is hydrostatic, the pressure can be eliminated from (27) to yield

$$\frac{\partial}{\partial z}\left(u\frac{\partial u}{\partial x} + w\frac{\partial u}{\partial z}\right) = \frac{\partial g'}{\partial x} - \frac{\partial^2}{\partial z^2}(\overline{u'w'}). \tag{28}$$

For the advective term $z \sim H$, and eliminating g' between (25) and (28), requiring the ratio of inertial and buoyancy terms in (28) to be independent of x, and recalling that $Q_- \sim uH$, leads to $u \sim (Bl)^{1/3}$, which is perfectly consistent with the experimentally supported scaling in (22) and (24) and confirms the derivation of (26) above. Note that

the coefficient in (22) implies that the inertial and buoyancy terms are of the same order of magnitude and that the coefficient was derived from the experimental data of figure 12.

On the other hand, for the buoyancy term to balance the Reynolds stress term requires

$$\overline{u'w'} \sim B^{2/3} l^{2/3} H/l. \tag{29}$$

If one were to introduce an eddy diffusivity K of the form

$$-\overline{u'w'} = K\frac{\partial u}{\partial z} \tag{30}$$

then clearly

$$K \sim B^{1/3} H^2/l^{2/3} \sim (BH)^{1/3} H(H/l)^{2/3} \tag{31}$$

which Garrett, Speer & Tragou (1995) and Tragou & Garrett (1997) pointed out was required by Phillips' approach. Note too the x-dependence implied by the buoyancy viscous balance from (28). What is curious about (31) is that written in this form, it is clear that it represents the product of the vertical turbulent velocity scale and the integral lengthscale of the turbulence under Rayleigh–Bénard convection, but multiplied by the aspect ratio to the power 2/3. It is hard to see a physical reason for this turbulent scaling, and indeed one would never anticipate this scaling from first principles using a mixing-length-type model. If we assume that (26) and (31) are valid, then clearly a three-way force balance of the boundary-layer type in the momentum equation is possible (i.e. of the type suggested by Phillips 1966) but the parameterization of the turbulence is not obvious by inspection. For example, from equation (29) one could assume that $u' \sim (BH)^{1/3}$ and $w' = (BH)^{1/3}(H/l)^{1/3}$, implying that the turbulence is anisotropic. It is clear that further work focused on making direct measurements of the turbulence field is required before these issues can be resolved.

In order to apply the scaling and results of this paper to field situations we require further information about the transport coefficients. For example, a minimal Rayleigh number for destabilizing forcing in the field, in say the sidearm of a lake, can be calculated by using $B_- \sim B_+ \sim O(10^{-8})$ m^2 s^{-3}, $l \sim O(10)^2$ m, $L \sim O(10)^3$ m, turbulent $\nu \sim \kappa \sim O(10^{-4})$ m^2 s^{-1} (if the turbulent Prandtl number is of $O(1)$) to result in a turbulent Rayleigh number of $O(10^{12})$. But what are the appropriate transport coefficients with which to calculate a corresponding Rayleigh number with stabilizing forcing? In the field the molecular coefficients are correct only in relatively rare instances when there is sustained dead calm, for turbulence can still dominate the surface layer even when there are strong stabilizing buoyancy fluxes (Imberger 1994). As an example of the significance of differing transport coefficients, consider equation (9), which can be applied to the field situation by re-deriving it while distinguishing between diffusivities appropriate to destabilizing and stabilizing forcing, resulting in

$$\frac{Q_-}{Q_{+I}} \sim \frac{Ra_-^{1/3}}{Ra_+^{1/6}} \frac{Pr_-^{1/2}}{Pr_+^{-3/4}} \frac{\kappa_-}{\nu_+} \frac{H}{l}. \tag{32}$$

Note that while the term $Pr_-^{1/2}/Pr_+^{-3/4}$ in (32) might be regarded as being merely of $O(1)$, the ratio κ_-/ν_+ is of $O(10^2)$ if one uses the value above for the turbulent coefficient in the destabilizing case and the molecular value for the stabilizing case. A physically interesting way of interpreting (9) is to note that $Q_- > Q_+$ provided that $H > \delta$, which will often be true in the field. Note that modest differences in the magnitude of the buoyancy flux will not strongly impair comparisons between the discharges from destablizing and stabilizing forcing as (see (2), (6) and (7)) $Q_- \propto B^{1/3}$ and $Q_+ \propto B^{1/6}$.

We can also compare the periods of destabilizing forcing employed in the experiments with the major flushing and filling-box scales and see how these, in turn, relate to physical time. For the example above of the sidearm of a lake, the forcing-region flushing time is given by (18) using a diurnal thermocline depth of 5 m for H, resulting in $\tau_f \sim 3 \times 10^4$ s (8 h) and the filling-box timescale is given by (19) so that $\tau_b \sim 5 \times 10^4$ s (15 h). These times confirm the importance of studying the unsteady flows, while allowing that steady-state flows can indeed be set up on a diurnal timescale. The ratios of the experimentally imposed periods of destabilizing forcing and the major timescales of the responses of the flow are $0.5 \leqslant \tau_-/\tau_F \leqslant 15$, $0.1 \leqslant \tau_-/\tau_b \leqslant 3.2$.

6. Concluding remarks

As a consequence of the application of a negative or destabilizing buoyancy flux at the water surface, unstable turbulent flows are created, while when the applied buoyancy flux is positive, stable laminar flows are generated. The inertia of the fluid is important when the flow is switched from forcing of one sign to the other. The finite time taken for the establishment of a fully recirculating convective region implies the importance of the forcing timescales, τ_- and τ_+, compared with the forcing-region flushing timescale τ_f and the filling-box timescale τ_b. A number of possible flow regimes have been identified depending on the ordering of these timescales. The time variation of the boundary conditions generates cavity-scale internal waves, which modify the flow in its approach to final steady state. The velocity of propagation of the front, established between mean counterflows and the fully turbulent region, in the transient regime with destabilizing forcing scales as $u_F \sim (BH)^{1/3}$ (see (14) and following). At steady state we find $Q_- = 0.2(Bl)^{1/3}H$ (equation (22)), which is in accord with prior suggestions. The discharge deriving from stabilizing forcing is $Q_{+I} \sim Ra_+^{1/6} Pr^{-3/4} \nu$ (equation (8a)), which was much less than Q_- in the experiments, demonstrating the importance of the flushing occurring during the destabilizing or cooling periods.

The authors thank M. Coates and C. Oldham and the anonymous reviewers who made useful comments on an earlier version of this paper, J. Devitt who constructed the experimental tank and assisted with experiments, and R. Weymouth who assisted with the experiments and helped process the data. This work is funded by the Australian Research Council. Centre for Water Research Reference ED-1198-JJS.

REFERENCES

Adrian, R. J., Ferreira, R. T. D. S. & Boberg, T. 1986 Turbulent thermal convection in wide horizontal fluid layers. *Exps. Fluids* **4**, 121–141.

Brocard, D. N. & Harleman, D. R. F. 1980 Two-layer model for shallow horizontal convective circulation. *J. Fluid Mech.* **100**, 129–146.

Burling, M. C., Ivey, G. N. & Pattiarachi, C. B. 1996 Natural convection in a shallow coastal embayment. *Continental Shelf Res.* (submitted).

Coates, M. C. & Patterson, J. C. 1993 Unsteady natural convection in a cavity with a non-uniform absorption of radiation. *J. Fluid Mech.* **256**, 133–161.

Fischer, H. B., List, E. J., Imberger, J. & Brooks, N. H. 1979 *Mixing in Inland and Coastal Waters*. Academic.

Garrett, C., Speer, K. & Tragou, E. 1995 The relationship between water mass formation and the surface buoyancy flux, with application to Phillips' Red Sea Model. *J. Phys. Oceanogr.* **25**, 1696–1705.

Imberger, J. 1994 Transport processes in lakes: a review. In *Limnology Now: A Paradigm of Planetary Problems* (ed. R. Margalef), pp. 99–193. Elsevier.

JAIN, S. C. 1982 Buoyancy-driven circulation in free-surface channels. *J. Fluid Mech.* **122**, 1–12.

MAXWORTHY, T. 1997 Convection into domains with open boundaries. *Ann. Rev. Fluid Mech.* **29**, 327–371.

MØLLER, J. S. 1984 Hydrodynamics of an arctic fjord. *Institute of Hydrodynamics and Hydraulic Engineering*, *Technical University of Denmark*, *Lyngby*, *Series Paper* 34.

MONISMITH, S., IMBERGER, J. & MORISON, M. L. 1990 Convective motions in the sidearms of a small reservoir. *Limnol. and Oceanogr.* **35**, 1676–1702.

PATTERSON, J. C. & ARMFIELD, S. W. 1990 Transient features of natural convection in a cavity. *J. Fluid Mech.* **219**, 469–497.

PHILLIPS, O. M. 1966 On turbulent convection currents and the circulation of the Red Sea. *Deep-Sea Res.* **13**, 1149–1160.

REIBLE, D. D., SIMPSON, J. E. & LINDEN, P. F. 1993 The sea breeze and gravity-current frontogenesis. *Q. J. R. Met. Soc.* **119**, 1–17.

STEVENS, C. S. & COATES, M. J. 1994 A maximised cross-correlation technique for resolving velocity fields in laboratory experiments. *J. Hydraul. Res.* 195–211.

STURMAN, J. J., IVEY, G. N. & TAYLOR, J. R. 1996 Convection in a long box driven by heating and cooling on the horizontal boundaries. *J. Fluid Mech.* **310**, 61–87.

TRAGOU, E. & GARRETT, C. 1997 The shallow thermohaline circulation of the Red Sea. *Deep-Sea Res.* **44**, 1355–1376.

TURNER, J. S. 1973 *Buoyancy Effects in Fluids*. Cambridge University Press.